J Mater Sci (2025) 60:3472–3483

Metals & corrosion

Effect of hot isostatic pressing on the low-cycle fatigue behavior of laser powder bed fusion manufactured 21-6-9 austenitic stainless steel

Ryosuke Ujiie[1,2,*], Magnus Neikter[2], Robert Pederson[2], Thomas Hansson[2,3], and Yukio Miyashita[1]

[1] *Department of Mechanical Engineering, Nagaoka University of Technology, Nagaoka 940-2188, Japan*
[2] *Department of Engineering Science, University West, 46132 Trollhattan, Sweden*
[3] *GKN Aerospace Sweden AB, 46181 Trollhattan, Sweden*

Received: 16 August 2024
Accepted: 15 January 2025
Published online: 21 January 2025

ABSTRACT

21-6-9 stainless steel manufactured by powder bed fusion (PBF-LB/M) is expected to be used for aerospace parts due to its high strength and elevated temperature durability, coupled with the possibility to manufacture complex shapes. Defects, such as pores and lack of fusion (LoF), can be formed in PBF-LB/M manufactured material, which can be detrimental to important dynamic mechanical properties like fatigue strength. However, hot isostatic pressing (HIP) has shown great potential in closing and healing such defects. In this study, an investigation of the effects of HIP treatment on the low-cycle fatigue (LCF) properties and microstructure of PBF-LB/M manufactured 21-6-9 material was performed. It was found that the effects of HIP treatment are similar to that of solution heat treatment regarding grain coarsening and grain sensitization. In addition, HIP successfully closed the pores, reducing the defect density. The stress relief heat-treated (SR) specimens exhibited lower LCF strength than wrought material, but after HIP treatment, LCF strength was equal to wrought material. The HIP treatment consequently improved the strain-controlled LCF strength but decreased the tensile strength and hardness around 30%.

Introduction

21-6-9 stainless steel is a nitrogen-strengthened austenitic stainless steel used for hydraulic tubes and aerospace engine components due to its high tensile strength, corrosion resistance, weldability, and elevated temperature durability [1, 2]. This alloy's nominal chemical composition is 21 wt% Cr, 6 wt% Ni, 9 wt% Mn, and 0.15–0.4 wt% N, with remaining Fe, and this composition is low in Ni content when compared with the 300 series of austenitic stainless steels. In general, a lower Ni content increases the solid

Handling Editor: Megumi Kawasaki.

Address correspondence to E-mail: s181013@stn.nagaokaut.ac.jp

E-mail Addresses: magnus.neikter@hv.se; robert.pederson@hv.se; thomas.hansson@hv.se; miyayuki@vos.nagaokaut.ac.jp

https://doi.org/10.1007/s10853-025-10654-7

solubility of N and increases the amount of stabilized austenite. As a result, high strength is achieved caused by the hindrance of dislocations due to nitrogen solid solution [3]. However, stainless steel has low machinability because of its high toughness and low thermal conductivity [4]. Machinability and high strength are contrary performances, and machinability has significantly affected the lead time and cost of the conventional manufacturing process of machining [5]. Therefore, manufacturing techniques that can enable more near-net-shape manufacturing are of high interest. This reduces the amount of machining needed to produce the final part geometry, which provides great potential in lowering total manufacturing costs and shortening lead times.

Metal powder used in powder bed fusion-laser beam (PBF-LB/M) is a metal additive manufacturing process in which metal powder is melted by a fast-moving laser heat source in a layer-by-layer procedure [6]. It offers a great level of potential in manufacturing near-net-shape geometrically complex components, coupled with a fine microstructure, rendering a material with good mechanical properties. The process works by first spreading a metal powder over the built plate using a recoater blade. Then, a laser beam selectively melts specific points of the powder bed according to a sliced 3D model. Once one layer has been processed, the build plate is lowered one layer thickness; then, the process repeats itself by raking out a new powder layer, followed by selective melting etc., until the required 2D layers render in the final 3D component. This process can build geometries with high accuracy and complex shapes but is consequently relatively costly and has a limited building rate [7]. However, if focused on manufacturing complex-shaped components, it can dramatically decrease the amount of post-build machining needed which, in turn, renders in minimal waste of material, thereby contributing to the reduction of CO_2 emissions and energy consumption throughout the manufacturing process. Within the aerospace industry, numerous components exist with complex shapes that potentially can take advantage of PBF-LB/M. For some of these critical applications, high material quality is required. To control the material quality in PBF-LB/M, some of the most important processing parameters are building direction and laser power [8–11]. Additive manufactured (AM) material quality is strongly dependent on the surface roughness, microstructure, and defects, which all can influence static and cyclic properties [12].

Defects, which can lead to local stress concentrations, risk acting as crack initiation points and thereby significantly reduce fatigue strength, this issue is also seen in PBF-LB/M materials [13, 14]. The most detrimental defect type in PBF-LB/M material is the lack of fusion (LoF) defects. The LoF defects can be minimized by adjusting the laser parameters and the building strategy. However, these process parameter changes, needed to avoid LoF defects, are not necessarily ideal measures when considering high productivity. Increasing the energy density by changing process parameters has been reported to reduce the defects, but this is accompanied by high power consumption and increased time for manufacturing [15–17]. Hot isostatic pressing (HIP) treatment effectively closes defects and optimizes the microstructure of AM-built material. Near-surface defects often act as crack initiation points, and it has been shown that fatigue strength was increased by HIP treatment by closing sub-surface defects [18]. However, it has been reported that HIP treatment of austenitic stainless steel may reduce yield strength and hardness due to grain coarsening caused by recrystallization [19]. Therefore, investigating the HIP treatment effects of the relationship between defects and fatigue life in AM materials is important before using this relatively new type of material in critical industrial applications.

In the present study, LCF testing was conducted and evaluated on stress relief heat-treated and HIP-treated 21-6-9 stainless steel material manufactured by PBF-LB/M. The objective was to characterize the fatigue behavior, fracture mechanism, and microstructure characteristics of both SR- and HIP-treated material.

Materials and method

Manufacturing process and powder

The 21-6-9 stainless steel material was manufactured using an SLM Solutions 125 machine, using 21-6-9 stainless steel powder with the nominal chemical composition as shown in Table 1. The powder was manufactured by Sandvik Additive Manufacturing using vacuum induction melting inert gas atomization. The powder has been passed through a 63 μm sieve with the following size distribution (obtained by

Table 1 Overview of chemical composition, powder, and as-build for 21-6-9 stainless steel

Wt %	C	Si	Mn	P	S	Cr	Ni	Mo	Cu	N
Powder	0.04	0.40	9.30	0.01	0.01	20.40	6.60	0.01	0.01	0.30
As build	0.05	0.36	8.74	0.01	0.01	20.21	6.46	< 0.01	0.02	0.27

laser diffraction): 21.2 µm (Dv10), 34.8 µm (Dv50), and 55.8 µm (Dv90). The powder characterization conforms to ASTM standard B822. The resulting chemical composition agrees with the UNS: S21900 and AMS5561 standards.

An inert argon gas atmosphere was used during the build, and the PBF-LB/M process parameters utilized were 180 W power, 900 mm/s scan speed, 30 µm layer thickness, and 0.14 mm hatch distance. The building strategy was striped, with 67 degrees of alternation between each deposited layer, and the built shapes were blanks and walls. Horizontal LCF specimens were machined out from the walls (the major axis is parallel to the build plate), while the vertical LCF specimens were perpendicular to the build plate. The build plate was made out of 316 stainless steel. After manufacturing, all specimens were cut from the build plate and heat treated at 600 °C, for 2 h, to relieve residual stresses [20]. After the stress relief heat treatment, selected specimens were HIP-treated according to the ASTM A1080.

Tensile properties and hardness

The HIPed specimens were evaluated using Vickers microhardness and tensile testing. The obtained tensile properties were compared with corresponding tensile properties from SR material [1]. Tensile testing was performed using a strain ratio of 0.8% sec^{-1}. Vickers microhardness measurements were performed using a Duramin-40 (Struers, Cleveland, OH, USA) machine with an applied load of 1 kg using a dwell time of 15 s. The microhardness measurements were conducted on the ground and polished material. Five randomly distributed indents were performed in the bulk material of each sample.

Low-cycle fatigue testing

LCF testing was performed by Metcut Research Inc (US) according to ASTM E606-19, on specimens with gauge section according to the sketch shown in Fig. 1 and using three types of specimens, stress relief heat-treated (SR) vertical, SR horizontal, and

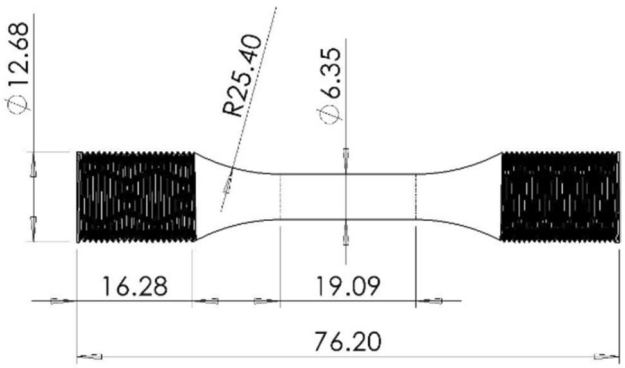

Figure 1 Sketch of the gauge section geometry used for LCF and tensile testing (in mm).

HIP-treated vertical. The HIP-treated horizontal specimen was excluded from the tests because it did not show any differences between vertical build and horizontal in the tensile test results described in Sect. "Tensile properties and hardness". Strain-controlled experiments were conducted in air at room temperature (RT), with a frequency of 0.5 Hz and an R-ratio of 0, for strain ranges between 0.5 and 2% using a triangular waveform. During the LCF testing, stress and strain were recorded for predetermined cycles to obtain hysteresis loops.

Fractography, defect, and microstructure characterization

Fractography was conducted using a scanning electron microscope (HITACHI TM3000, acceleration voltage = 1.5 kV). Observation of microstructure and porosity was performed using an optical microscope (ZEISS AX10). The fractographic study was focused on investigating the crack initiation site and to characterize the fracture surface. Specimens were cut parallel and perpendicular to the build direction and polished for observation of defects, and the defect fraction was calculated using ImageJ (the area density of the solid area was measured by binarizing the area of defects and solid areas). After this, specimens were electrolytically etched (oxalic acid 10%, 3 V, 50 s) for observation of grain boundaries, followed by

additional etching of 100 s and 300 s, for observation of sub-grains. Grain size measurement was conducted according to the ASTM standard E112-13, by drawing straight lines and circles, and counting intercepts.

Result

Tensile properties and hardness

The tensile properties and microhardness measurements are summarized in Table 2. For comparison, corresponding properties for SR vertical and SR horizontal material from [1] are also included. However, HIPed material showed significant differences in both tensile strength and hardness compared to SR material, as shown in Table 2. No significant directional difference in tensile properties and hardness for the SR material was found.

Low-cycle fatigue testing

Figure 2 shows strain range versus number of cycles to failure comparisons for HIPed vertical, SR vertical, and SR horizontal. The failure was determined as the cycle for which 50% load range drop from the stable load range was measured. HIPed vertical specimens exhibited the highest LCF life followed by SR horizontal specimens and SR vertical specimens. HIPed vertical showed an LCF life comparable to that

Table 2 Microhardness and tensile properties of PBF-LB/M build material, SR vertical, and horizontal results are taken from [1], and wrought annealed properties are taken from [21]

	Tensile strength	0.2% Proof stress	Young's modulus	Elongation	Reduction of area	Hardness
SR Vertical	825 MPa	620 MPa	192 GPa	42%	46%	272 HV ± 6
SR Horizontal	820 MPa	620 MPa	188 GPa	44%	51%	270 HV ± 7
HIPed Vertical	544 MPa	333 MPa	170 GPa	–	63%	189 HV ± 6
Wrought annealed	655 MPa	330 MPa	196 GPa	35%	–	–

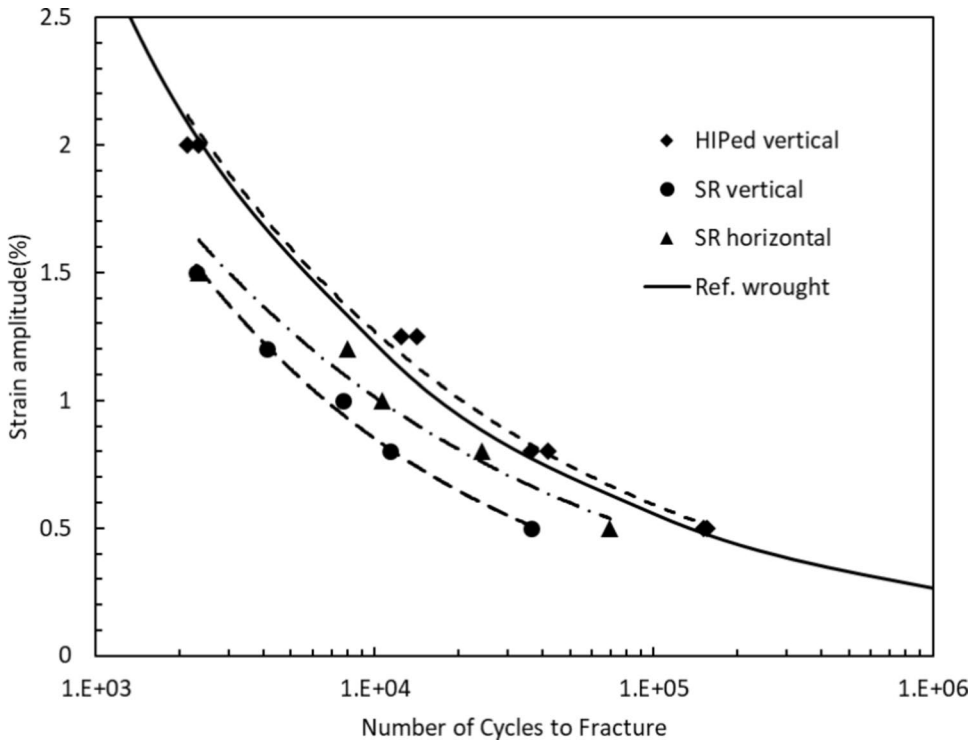

Figure 2 Comparison of LCF life for HIPed vertical, SR vertical, SR horizontal, and reference properties for wrought [22].

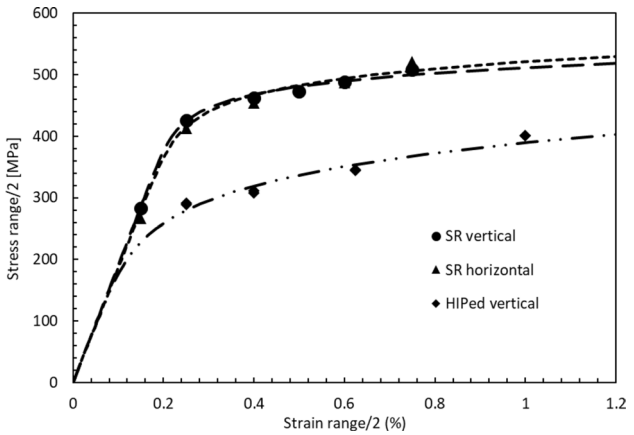

Figure 3 Cyclic stress–strain curves for SR vertical and horizontal and HIPed vertical.

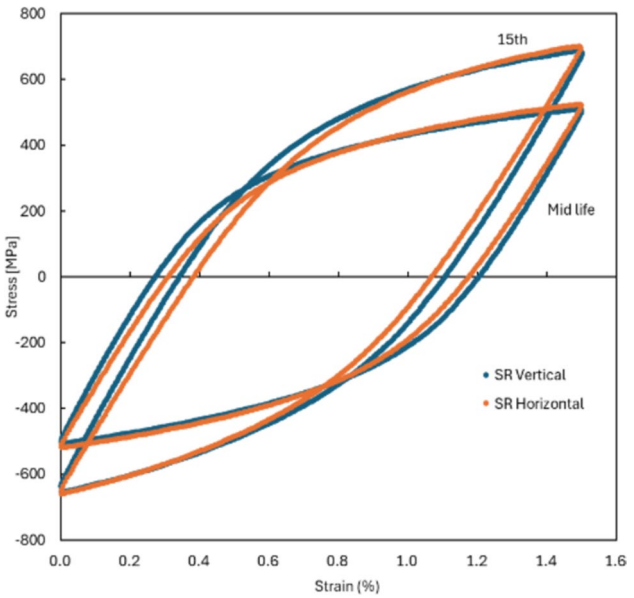

Figure 4 Stress–strain plot of the 15th cycle and mid-life under LCF testing of SR material; vertical direction shows more plastic strain than the horizontal direction. In addition, Young's modulus is somewhat different in the two directions.

of wrought material annealed at 1100 °C for 30 min [22]. The cyclic stress–strain curves are shown in Fig. 3. SR vertical specimens and SR horizontal specimens showed no significant difference while the HIPed vertical specimens showed a significantly lower stress range.

Hysteresis loop

Since the tests did not reach the desired strain for the first few cycles of the LCF test, the hysteresis loop for the first cycle reaching the required strain range for all tests, cycle 15, was used and is shown in Fig. 4. The tensile tests show no difference between vertical and horizontal directions, but measured from the LCF cycles the tensile properties are different especially the Young's modulus. Young's modulus was measured from the linear behavior part of the hysteresis loops in Fig. 4. In the vertical direction, it is 189 GPa and in the horizontal 167 GPa. This directional difference in Young's modulus was observed for all tested strain ranges. Therefore, the anisotropic LCF life and cyclic stress–strain are believed to be related to the corresponding Young's modulus difference. The plastic strain was obtained by subtracting the elastic strain range from the total strain range of the hysteresis loops in Fig. 4. A comparison between SR vertical and SR horizontal is summarized in Fig. 5. The test specimens in the vertical direction recorded more plastic strain than in the horizontal direction, for all tested strain ranges.

Fractography

The fracture surfaces of the LCF specimens were investigated, and crack initiation sites and crack propagation surfaces were identified, characterized, and compared. Figure 6 shows that the LCF test specimen fracture surfaces of SR vertical, SR horizontal, and HIPed, respectively, tested at a strain range of 0.5%. The crack propagation region of the HIPed material was smoothest (Fig. 6a), followed by a rougher crack propagation region in the SR horizontal specimen (Fig. 6c), and with the roughest crack propagation region found in the SR vertical specimen (Fig. 6b). On the fracture surfaces of the SR specimens, steps were observed.

Figure 7 shows defects observed in the vicinity of the large steps on the fracture surfaces of, a–c SR vertical specimen tested at a strain range of $\Delta\varepsilon = 1.0\%$, d SR vertical specimen tested at a strain range of $\Delta\varepsilon = 0.8\%$, and e SR vertical specimen tested at a strain range of $\Delta\varepsilon = 0.5\%$. These types of defects were more prevalent in vertical specimens and mainly located on the rough fatigue fracture surfaces in the vicinity of large steps. In addition, these types of defects were

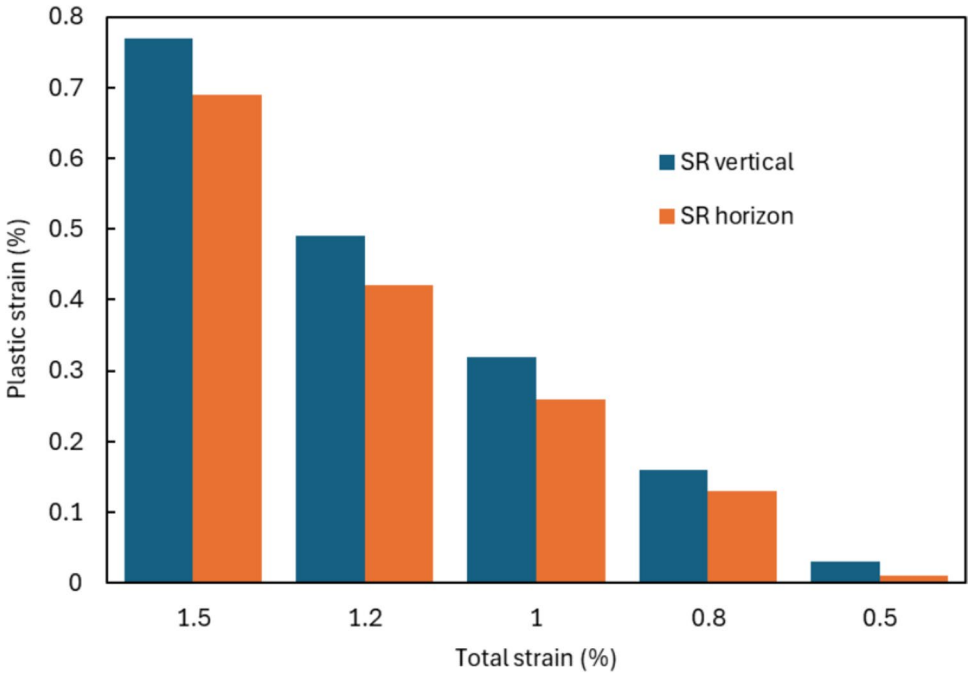

Figure 5 Plastic strain extracted from hysteresis loops of the 15th cycle under LCF testing—Vertical direction shows more plastic strain at all strain ranges tested.

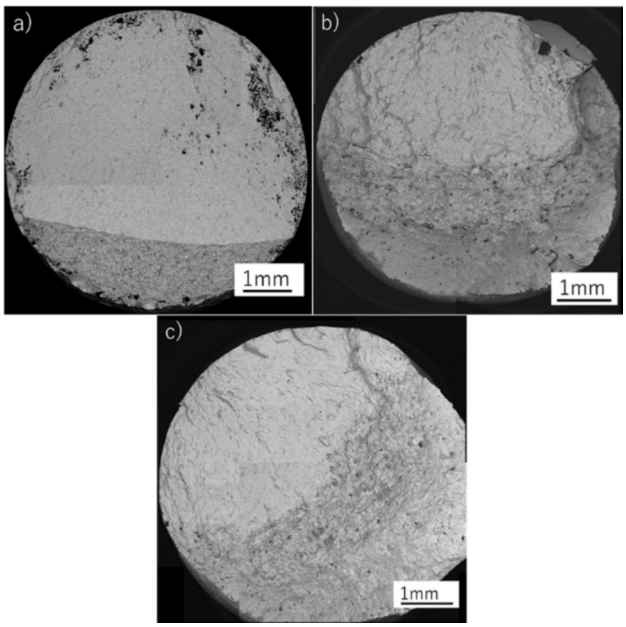

Figure 6 Fracture surfaces of the LCF specimens tested at a strain–strain range of 0.5%, **a** HIPed vertical, **b** SR vertical, and **c** SR horizontal.

observed on fracture surfaces of vertical specimens tested at all strain ranges.

Figure 8 summarizes different crack initiation points found. Different fatigue crack initiation locations were identified in SR and HIPed LCF specimens. Figure 8a shows the crack initiation at a surface defect in SR vertical specimen tested at a strain range of $\Delta\varepsilon = 0.8\%$, b and c shows the sub-surface crack initiation sites at LoF defects in SR specimens tested at strain ranges of $\Delta\varepsilon = 0.5\%$ and $\Delta\varepsilon = 0.3\%$, respectively. Figures d and e show the crack initiation region of HIPed specimens tested at strain ranges of $\Delta\varepsilon = 1.25$ and $\Delta\varepsilon = 0.8$, respectively, and in both cases crack initiation seemed not to be related to defects as opposed to the SR specimens.

Observation of microstructure and defects

The amount of defects measured in the SR and HIPed materials are summarized in Fig. 9. The plane parallel to the build direction is the horizontal cross-section, and the perpendicular to the build direction is the vertical cross-section. Defect density was found to decrease after HIP treatment.

The microstructure of the SR material is shown in Fig. 10a after a 50 s etching, while the HIPed material needed a longer etching time of 300 s in order to reveal the microstructure shown in Fig. 10c. The HIPed material consisted of equiaxed grain morphology of an average size of 26.5 μm with some twinned grains as well, while SR material showed an equiaxed grain distribution of an average grain size of 13.2 μm.

SR specimen sub-grains are shown in Fig. 11, the black dotted markings exemplify a grain. Within each

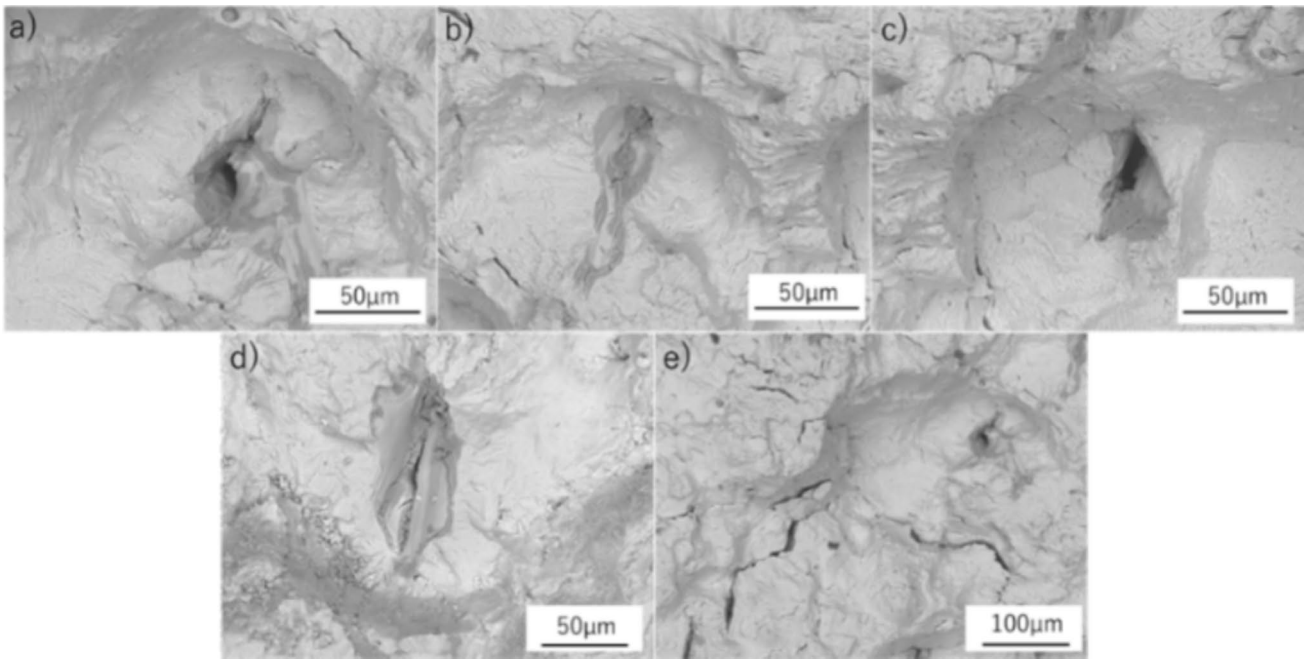

Figure 7 Defects on fracture surfaces near steps, on specimens **a**–**c** SR vertical specimen tested at a strain range of $\Delta\varepsilon = 1.0\%$, **d** SR vertical specimen tested at a strain range of $\Delta\varepsilon = 0.8\%$, and **e** SR vertical specimen tested at a strain range of $\Delta\varepsilon = 0.5\%$.

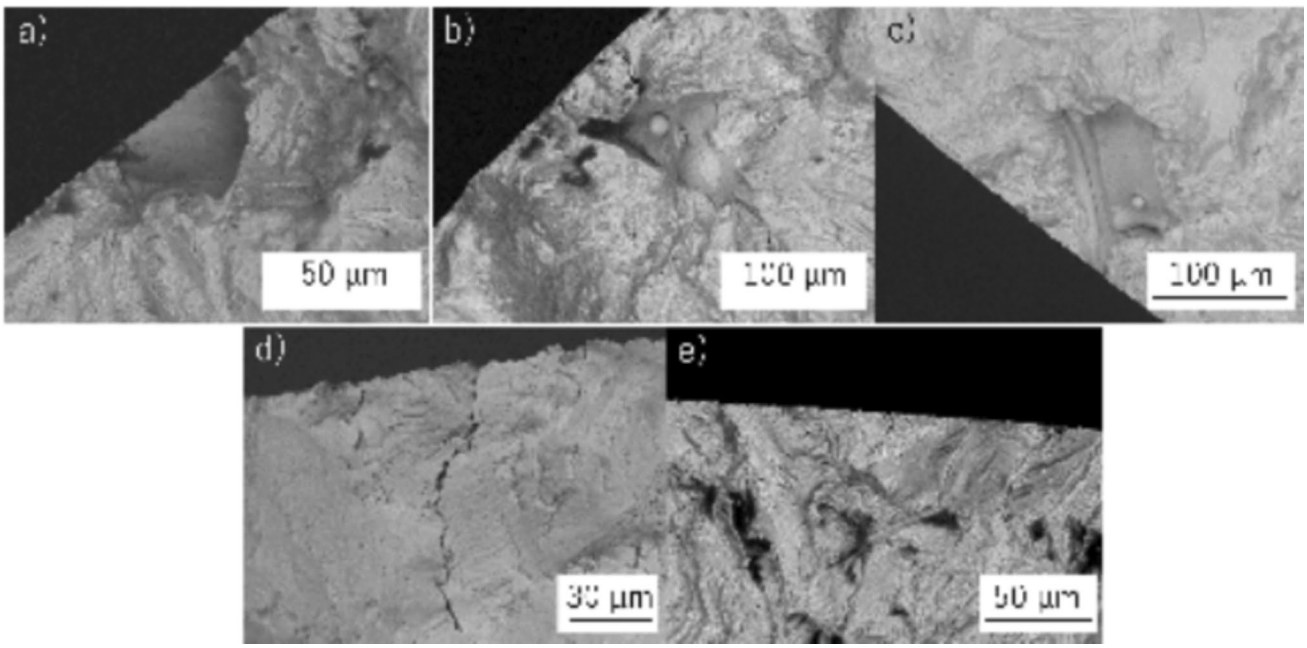

Figure 8 Fatigue crack initiation locations identified in SR and HIPed LCF specimens. **a** shows the crack initiation at a surface defect in SR vertical, $\Delta\varepsilon = 0.8\%$, **b** and **c** shows the sub-surface crack initiation sites at LoF defects in SR, $\Delta\varepsilon = 0.5\%$ and $\Delta\varepsilon = 0.3\%$, respectively. **d** and **e** shows the crack initiation region of HIPed specimens, $\Delta\varepsilon = 1.25$ and $\Delta\varepsilon = 0.8$.

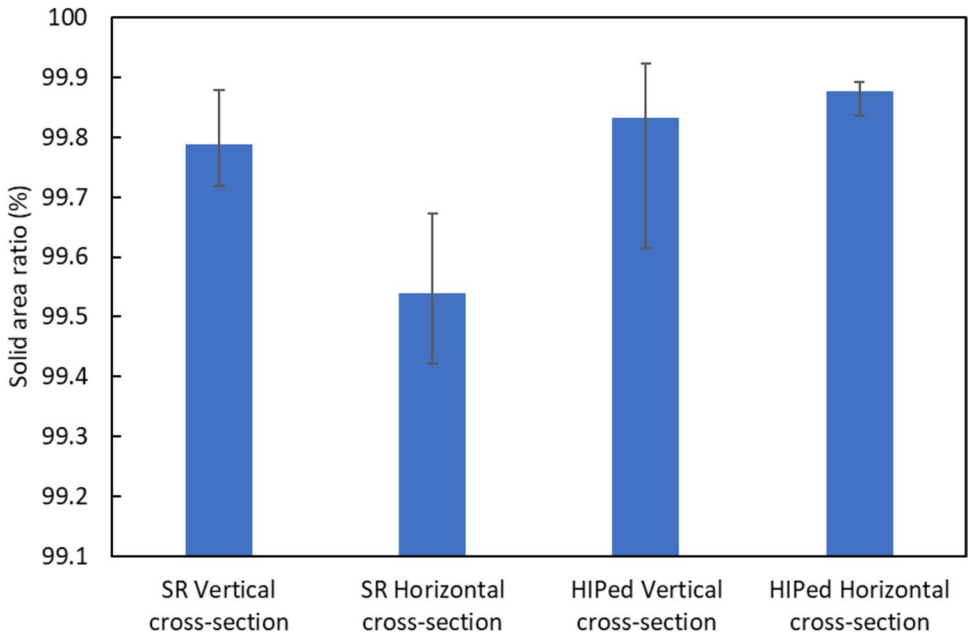

Figure 9 Summary of internal defect density measured in SR and HIPed material.

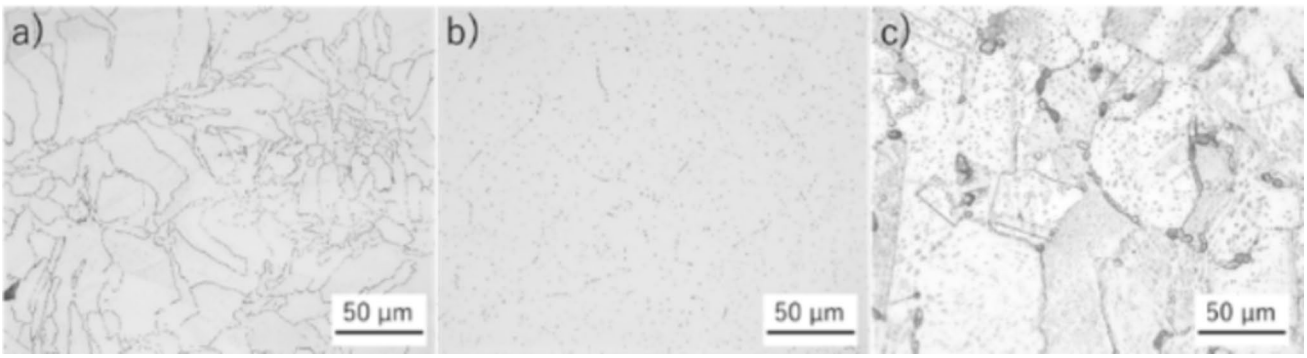

Figure 10 In **a** the etching 50 s result of SR vertical is shown, in **b** 50 s HIPed vertical, and **c** 300 s HIPed vertical. In **a** the etching revealed the microstructure, whereas in the corresponding etching in **b** the HIPed did not reveal the microstructure. For **c**, the etching revealed grain boundaries.

grain, there were numerous so-called sub-grains with a cellular morphology. SR specimens grain boundaries were preferentially corroded in the 50 s and then, the whole area was corroded in the 100 s, and sub-grains could be seen clearly. This sub-grain is commonly found in welds and PBF-LB/M of steel materials and is formed by rapid cooling after melting.

Discussion

Fatigue properties

Figure 3 shows that there is no significant difference in the cyclic stress–strain curves for horizontal and vertical SR materials. Table 2 shows that there is no difference in microhardness and tensile properties, and both vertical and horizontal SR material exhibited crack initiation at sub-surface defects. However, Fig. 2 shows that the LCF life is higher for the horizontal direction. The reason for this could be that the vertical specimens exhibit a higher percentage of plastic strain as compared with the horizontal specimens, at the

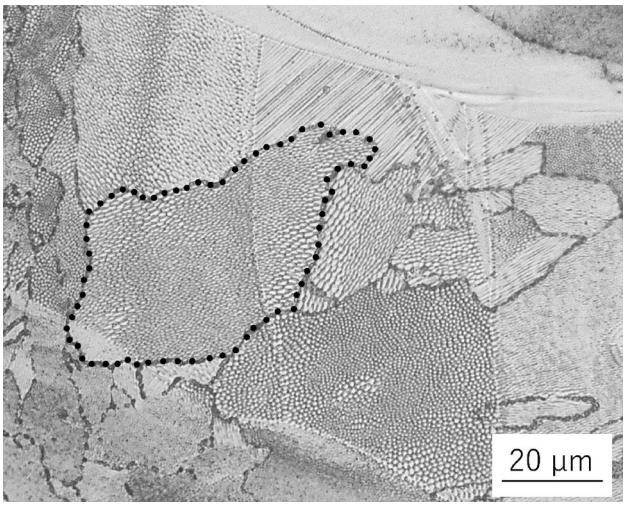

Figure 11 The SR material that was exposed to a 100 s etching. The black-dotted markings exemplify a grain. Within each grain, there were numerous so-called sub-grains with a cellular morphology.

same strain ranges which is depicted in Fig. 5. With increased plastic deformation the dislocation density also increases, which then accumulates and eventually leads to crack initiation [23].

In the present study, it was found that Young's modulus varied with orientation, i.e., was anisotropic. This aligns well with previous studies of austenitic stainless steels manufactured by PBF-LB/M, where it has been reported to have slight anisotropy in physical properties due to preferred crystallographic orientation [24]. From the electron backscatter diffraction (EBSD) results in [1], the texture obtained showed a slightly preferred crystallographic texture and the multiple of random distribution (MRD) for the horizontal cross-section was 3.64, while for the vertical cross-Sect. 3.97.

In some of the fracture surfaces of SR material, large steps were found, indicating that cracks propagated from multiple sites and then linked up with the main crack. While crack meanders are generally influenced by grain boundaries and slip bands, PBF-LB/M has internal defects that are larger than the microstructural scale, and stress concentrations can affect crack propagation. Therefore, it is suggested that the main crack that propagates in the vicinity of a defect may propagate rapidly toward the defect at the stress concentration near the defect. Secondary cracks have also been reported to initiate from defects and merge with the main crack, suggesting that any reduction in the crack growth life is due to the formation of a rough fracture surface [25]. Figure 7 shows a lack of fusion defects identified near the step in the fatigue fracture surface of the SR vertical, which may have caused the crack to propagate preferentially toward the defect and crack growth to occur rapidly near the defects. The large number of defects observed on the fracture surface suggests that the crack propagated from defect to defect, which may increase the crack growth rate [26]. Since cracks propagate preferentially in the direction of high stress, the stress concentration near the defect is considered to have caused the coalescence of the defect and the crack. The horizontal specimen's fracture surfaces are smooth because the crack lines up with fewer defects. This result suggests the non-uniform distribution of SR defects. It is a possibility supported by the large area of defects on the SR horizontal cross-section in Fig. 9.

Comparing HIPed vertical and SR vertical specimens, the LCF life was predominantly improved by HIP treatment, as shown in Fig. 2. However, the stress response for the same strain range for the HIPed condition was lower than the SR. The decrease in tensile strength and hardness is clearly shown in Table 2, indicating that the ductility is greatly improved. In general, ductility has a major effect on fatigue life, and with improved ductility, the LCF life is also expected to improve [27]. Figure 8d and e show that crack initiation in HIPed material did not occur from defects, as in SR material, suggesting a reduction of defects by HIP treatment.

Microstructure

The decrease in tensile strength and hardness because of the HIP treatment can be due to the increase in grain size from 13.2 to 26.5 µm. In particular, the SR specimens are heated and cooled rapidly by the PBF-LB/M process, and the grain size is smaller than that obtained by conventional processes like cast and wrought. The sub-grains in Fig. 11 are structures that are generally formed by rapid solidification due to rapid cooling during the PBF-LB/M process [28]. The PBF-LB/M material has higher tensile strength than that obtained through the relationship between grain size and tensile strength shown by the Hall–Petch relationship in [29], suggesting that the presence

of sub-grains is the cause. From M.E. Kassner et al. [30], 21-6-9 stainless steel's Hall–Petch relationship equation is,

$$\sigma_y = 282 + \frac{503}{\sqrt{d}} \quad (1)$$

(σ_y is the yield strength [MPa], d is the average grain size [μm]). From Eq. 1, applying the average grain size obtained in this study, the respective calculated yield stresses are 420 MPa for SR and 380 MPa for HIPed. The calculated yield stresses are lower for the SR than for the experimental value 620 MPa where sub-grains are observed. Therefore, decreased tensile strength and hardness in HIPed material are considered to be caused by two phenomena: grain size coarsening and sub-grain elimination [29, 30]. In addition, grain coarsening is known to increase ductility, and as discussed in Sect. "Fatigue properties", the increased LCF strength of HIPed specimens is explained by this phenomenon.

The morphology of the microstructures after HIP is similar to that after solution treatment [31]. Solution treatment is usually performed between 1000 and 1200 °C, and the HIP process used in this study was performed at around 1200 °C. Therefore, it is considered that the effect of HIP is similar to that of the solution treatment.

The grain boundaries of the SR specimens were easily corroded, suggesting sensitization due to chromium carbide precipitation. When austenitic stainless steels are held between 600 and 800 °C, [32] chromium carbide precipitation occurs at the grain boundaries, and the grain boundaries' corrosion resistance is significantly reduced. The SR specimens are considered to have heat-affected zones (HAZs) during the PBF-LB/M process, even in areas after solidification, and the entire specimen appears like a welded HAZ[33], suggesting that the specimens were held for a certain time during the building process at temperatures at which chromium carbide precipitation could occur (see Fig. 10)[34].

In summary, the SR material has higher tensile strength and microhardness than HIPed material, due to grain refinement, but observed grain sensitization induced by the PBF-LB/M manufacturing process. The HIP treatment reduces internal defects while solving grain sensitization by the dissolution of chromium carbides and reduces tensile strength and microhardness because of inherent grain growth.

Conclusion

The fatigue properties of PBF-LB/M manufactured 21-6-9 stainless steel material in SR and HIPed conditions have been investigated. The main conclusions are summarized as follows:

- HIP treatment reduced defect content and increased ductility. This resulted in reduced fatigue crack initiation from defects and increased LCF strength equivalent to wrought material.
- HIPed specimens did not show crack initiation from defects, and defects were not found on the fatigue fracture surface.
- The SR material has superior tensile strength and hardness, but the LCF strength is inferior to that of wrought materials and HIPed material, and Young's modulus and LCF strength were anisotropic.
- HIP treatment eliminates grain boundary sensitization inherited from the PBF-LB/M manufacturing process.

Acknowledgements

This research was funded by Västra Götalandsregionen, Tillväxtverket, European Regional Development Fund, and GKN Aerospace Sweden AB through the Spacelab project (Grant number 20201639).

Author contribution

Ryosuke Ujiie was contributed writing—review and editing, writing—original draft, data curation, formal analysis, and investigation. Magnus Neikter was involved in writing—review and editing, supervision, conceptualization, and project administration. Robert Pederson was performed writing—review and editing. Thomas Hansson was done writing—review and editing, and conceptualization. Yukio Miyashita did writing—review and editing and supervision.

Funding

Open access funding provided by Nagaoka University of Technology.

Data availability

Due to the ongoing nature of this project, we do not wish to share any data right now.

Declarations

Conflict of interest The authors have no known competing financial interests or personal relationships that could have appeared to influence the work reported in this paper.

References

[1] Neikter M, Edin E, Proper S, Bhaskar P, Nekkalapudi GK, Linde O, Hansson T, Pederson R (2021) Tensile properties of 21-6-9 austenitic stainless steel built using laser powder-bed fusion. Mater 14(15):4280

[2] Elmer JW, Ellsworth GF, Florando JN, Golosker IV, Mulay RP (2017) "Microstructure and mechanical properties of 21-6-9 stainless steel electron beam welds. Metall Mater Trans A 48(4):1771–1787

[3] Simmons JW (1996) Overview: high-nitrogen alloying of stainless steels. Mater Sci Eng A 207:159–169

[4] Akasawa T, Sakurai H, Nakamura M, Tanaka T, Takano K (2003) Effects of free-cutting additives on the machinability of austenitic stainless steels. J Mater Process Technol 143–144:66–71

[5] Hoier P, Malakizadi A, Friebe S, Klement U, Krajnik P (2019) Microstructural variations in 316L austenitic stainless steel and their influence on tool wear in machining. Wear 428–429:315–327

[6] M. Neikter, Microstructure and hydrogen embrittlement of additively manufactured Ti-6Al-4V, *Luleå University of Technology*, 2019

[7] Khorasani M, Gibson I, Ghasemi AH, Hadavi E, Rolfe B (2023) Laser subtractive and laser powder bed fusion of metals: review of process and production features. Rapid Prototyp J 29(5):935–958

[8] Snyder JC, Thole KA (2020) Understanding laser powder bed fusion surface roughness. J Manuf Sci Eng 142(7):071003

[9] Calignano F (2018) Investigation of the accuracy and roughness in the laser powder bed fusion process. Virtual Phys Prototyp 13(2):97–104

[10] Oliveira JP, LaLonde AD, Ma J (2020) Processing parameters in laser powder bed fusion metal additive manufacturing. Mater Des 193:108762

[11] Matthews MJ, Guss G, Khairallah SA, Rubenchik AM, Depond PJ, King WE (2016) Denudation of metal powder layers in laser powder bed fusion processes. Acta Mater 114:33–42

[12] Acharya R, Sharon JA, Staroselsky A (2017) Prediction of microstructure in laser powder bed fusion process. Acta Mater 124:360–371

[13] Romano S, Nezhadfar PD, Shamsaei N, Seifi M, Beretta S (2020) High cycle fatigue behavior and life prediction for additively manufactured 17–4 PH stainless steel: effect of sub-surface porosity and surface roughness. Theor Appl Fract Mech 106:102477

[14] Masuo H, Tanaka Y, Morokoshi S, Yagura H, Uchida T, Yamamoto Y, Murakami Y (2017) Effects of defects, surface roughness and HIP on fatigue strength of Ti-6Al-4V manufactured by additive manufacturing. Procedia Struct Integr 7:19–26

[15] Guo Q, Zhao C, Escano LI, Young Z, Xiong L, Fezzaa K, Everhart W, Brown B, Sun T, Chen L (2018) Transient dynamics of powder spattering in laser powder bed fusion additive manufacturing process revealed by in-situ high-speed high-energy x-ray imaging. Acta Mater 151:169–180

[16] Yin J, Wang D, Yang L, Wei H, Dong P, Ke L, Wang G, Zhu H, Zeng X (2020) Correlation between forming quality and spatter dynamics in laser powder bed fusion. Addit Manuf 31:100958

[17] Ali U, Esmaeilizadeh R, Ahmed F, Sarker D, Muhammad W, Keshavarzkermani A, Mahmoodkhani Y, Marzbanrad E, Toyserkani E (2019) Identification and characterization

of spatter particles and their effect on surface roughness, density and mechanical response of 17–4 PH stainless steel laser powder-bed fusion parts. Mater Sci Eng A 756:98–107

[18] Masuo H, Tanaka Y, Morokoshi S, Yaguro H, Uchida T, Yamamoto Y, Murakami Y (2018) Influence of defects, surface roughness and HIP on the fatigue strength of Ti-6Al-4V manufactured by additive manufacturing. Int J Fatigue 117:163–179

[19] Liverani E, Lutey AHA, Ascari A, Fortunato A (2020) The effects of hot isostatic pressing (HIP) and solubilization heat treatment on the density, mechanical properties, and microstructure of austenitic stainless steel parts produced by selective laser melting (SLM). Int J Adv Manuf Tech 107:109–122

[20] Edin E, Svahn F, Neikter M, Åkerfeldt P (2023) Stress relief heat treatment and mechanical properties of laser powder bed fusion built 21-6-9 stainless steel. Mater Sci Eng A 868:144742

[21] METEK, finetubes, *Stainless steel Alloy 21-6–9 Technical data sheet*, vol. V2.10.23.

[22] Hennessy D, Steckel G, Altstetter C (1967) Phase transformation of stainless steel during fatigue. Metall Trans A 7:415–424

[23] Sangid MD (2013) The physics of fatigue crack initiation. Int J Fatigue 57:58–72

[24] Charmi A, Falkenberg R, Avila L, Mohr G, Sommer K, Ulbricht A, Sprengel M, Neumann RS, Skrotzki B, Evans A (2021) Mechanical anisotropy of additively manufactured stainless steel 316L: an experimental and numerical study. Mater Sci Eng A 799:140154

[25] Xu Z, Liu A, Wang X, Liu B, Guo M (2021) Fatigue limit prediction model and fatigue crack growth mechanism for selective laser melting Ti6Al4V samples with inherent defects. Int J Fatigue 143:106008

[26] Tarik Hasib M, Ostergaard HE, Li X, Kruzic JJ (2021) Fatigue crack growth behavior of laser powder bed fusion additive manufactured Ti-6Al-4V: roles of post heat treatment and build orientation. Int J Fatigue 142:105955

[27] Ye D, Matsuoka S, Nagashima N, Suzuki N (2006) The low-cycle fatigue, deformation and final fracture behaviour of an austenitic stainless steel. Mater Sci Eng A 415(1–2):104–117

[28] Liu L, Ding Q, Zhong Y, Zou J, Wu J, Chiu YL, Li J, Zhang Z, Yu Q, Shen Z (2018) Dislocation network in additive manufactured steel breaks strength–ductility trade-off. Mater Today 21(4):354–361

[29] Hong Y, Zhou C, Zheng Y, Zhang L, Zheng J (2021) The cellular boundary with high density of dislocations governed the strengthening mechanism in selective laser melted 316L stainless steel. Mater Sci Eng A 799:140279

[30] Kassner ME, Geantil P (2012) Yield stress of 21-6-9 stainless steel over very wide ranges of strain rates and temperatures. J Mater Eng Perform 21(1):69–73

[31] Spruiell JE, Scott JA, Ary CS, Hardin RL (1973) Microstructural stability of thermal-mechanically pretreated type 316 austenitic stainless steel. Metall Trans 4:1533–1544

[32] Parvathavarthini N, Dayal RK, Khatak HS, Shankar V, Shanmugam V (2006) Sensitization behaviour of modified 316N and 316L stainless steel weld metals after complex annealing and stress relieving cycles. J Nucl Mater 355(1–3):68–82

[33] Ragavendran M, Vasudevan M (2020) Laser and hybrid laser welding of type 316L(N) austenitic stainless steel plates. Mater Manuf Processes 35(8):922–934

[34] Ganesh P, Giri R, Kaul R, Sankar PR, Tiwari P, Atulkar A, Porwal RK, Dayal RK, Kukreja LM (2012) Studies on pitting corrosion and sensitization in laser rapid manufactured specimens of type 316L stainless steel. Mater Des 39:509–521